

Direct imaging of spatial heterogeneities in type II superconductors

Donald M. Evans^{1,2,*}, Michele Conroy³, Lukas Puntigam¹, Dorina Croitori⁴, Lilian Prodan¹, James O. Douglas³, Baptiste Gault^{3,5}, and Vladimir Tsurkan^{1,4}

¹ Experimental Physics V, Center for Electronic Correlations and Magnetism, Institute of Physics, University of Augsburg, Augsburg 86159, Germany.

² Department of Physics, University of Warwick, Coventry CV4 7AL, UK.

³ Department of Materials, Imperial College London, London SW7 2AZ, UK.

⁴ Institute of Applied Physics, Moldova State University, Chisinau, Moldova.

⁵ Max-Planck-Institut für Eisenforschung GmbH, Max-Planck-Straße 1, Düsseldorf 40237, Germany.

*E-mail: donald.evans@uni-a.de

Abstract:

Understanding the exotic properties of quantum materials, including high-temperature superconductors, remains a formidable challenge that demands direct insights into electronic conductivity. Current methodologies either capture a bulk average or near-atomically-resolved information, missing direct measurements at the critical intermediate length scales. Here, using the superconductor Fe(Se,Te) as a model system, we use low-temperature conductive atomic force microscopy (cAFM) to bridge this gap. Contrary to the uniform superconductivity anticipated from bulk assessments, cAFM uncovers micron-scale conductive intrusions within a relatively insulating matrix. Subsequent compositional mapping through atom probe tomography, shows that differences in conductivity correlated with local changes in composition. cAFM, supported by advanced microscopy and microanalysis, represents a methodological breakthrough that can be used to navigate the intricate landscape of high-temperature superconductors and the broader realm of quantum materials. Such fundamental information is critical for theoretical understanding and future guided design.

Introduction

High temperature superconductors represent a vibrant frontier in condensed matter physics due to their revolutionary technological potential and the unconventional properties challenging traditional understanding based on Bardeen-Cooper-Schrieffer (BCS) theory.¹⁻³ The general assumption in solid-state science is that properties deduced from bulk measurements can be extrapolated to the unit cell scale. The challenges of this maxim are epitomised by the recent

surge of (public) interest in reports of apparent room temperature superconductivity in LK-99.^{4,5} Initial reports from bulk measurements suggested the existence of the Meissner effect (via, e.g., magnetic levitation) and zero-electrical-resistivity at room temperature and pressure.^{6,7} It is now widely believed that these bulk properties originated from an unexpected secondary phase.⁸

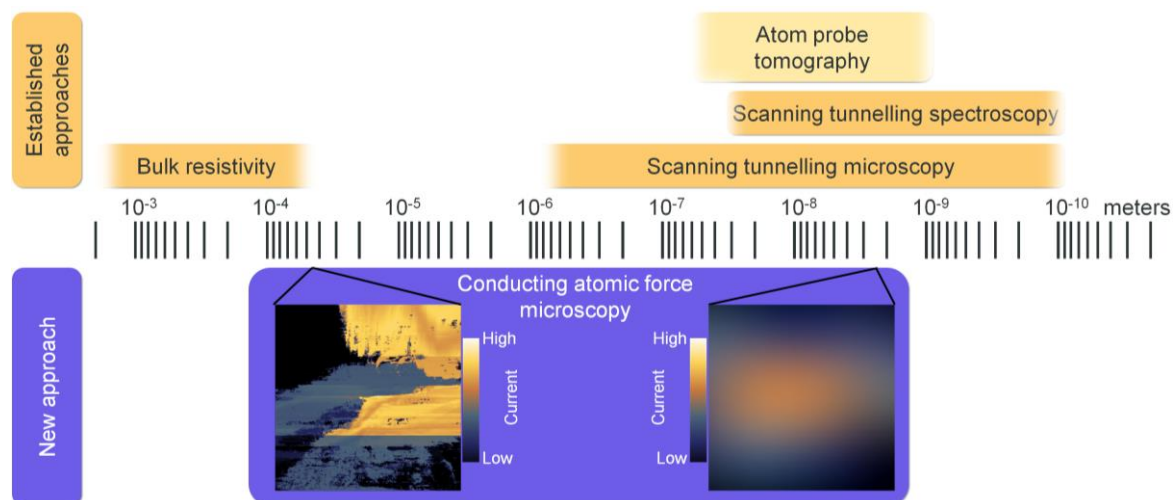


Figure 1 | Schematic of measurement length scales. The techniques in yellow illustrate established measurement techniques and their operational length scales. Atom probe tomography is in lighter yellow to highlight it measures composition rather than properties. The blue illustrates the new approach of using cAFM on superconductors, the left insert is a 35 x 35 μm area, while the right insert shows a 15 x 15 nm area.

A hallmark of superconductivity is its zero D.C. resistance, which is typically ascertained through bulk 4-probe electrical characterisation, thereby providing an aggregate view, i.e. not spatially resolved. Spatially-resolved electronic properties in superconductors come from scanning tunnelling microscopy (STM) and scanning tunnelling spectroscopy (STS).⁹⁻¹² Powerful as these are, neither provides direct measurements of conductivity *per se*, rather giving information of the surface density of states (DOS) of a single atomic site, and spectroscopy data is typically only presented up to a tens of nanometre scale.¹³⁻¹⁶ This means that many electronic properties must be extrapolated from those inferred at atomic scale measurements of surface DOS up to the conductivity observed in bulk crystals, schematically illustrated in Figure 1. Unfortunately, the length scale with a lack of direct imaging of conducting properties is exactly those where microstructural elements like precipitates, grain and twin boundaries, stacking faults, dislocations, and compositional and structural nuances are known to play crucial roles in functionality.¹⁷⁻²⁰

This study focuses on the well known superconductor $\text{Fe}(\text{Se}_{0.4\pm\alpha}, \text{Te}_{0.6\pm\beta})$ which has the peak transition temperature of $\sim 14.5 \text{ K}$,^{21,22} and inherent atomic scale disorder as the Se and Te ions reside in identical Wyckoff positions but at varying heights.^{11,22-24} It is chosen because it

has been previously characterised by a majority of state-of-the-art techniques, with reports of multiband superconductivity,^{25,26} a distinctly low and inhomogeneous superfluid density,^{12,27} claims of Majorana zero-mode states,^{28,29} topological superconductivity,^{30,31} and intriguing observations of spatially varying (in-)gap states.^{11,32} In addition, theoretical consideration suggests it is at the nexus of two theories to describe the pairing interactions, BCS- and Bose-Einstein condensate theories, making it inherently interesting.^{33,34}

In this study, we utilize conductive atomic force microscopy (cAFM), a technique that offers a spatially resolved, holistic view of currents across numerous atomic interactions, rather than showing the local DOS at the surface. Capable of spanning four orders of magnitude in a single image, cAFM reveals that in $\text{Fe}(\text{Se}_{0.4\pm\alpha}, \text{Te}_{0.6\pm\beta})$, superconductivity is confined to specific micron-scale regions. This is in direct contrast to our expectations from bulk measurements, where such spatial inhomogeneities are invisible. Moving beyond this revelation, cAFM is synergistically combined with atom probe tomography (APT), to provide atomic-scale 3D compositional mapping of these different regions. This gives a direct link between electronic properties and specific chemical composition, essential for accurate theory development. CAFM based multiscale characterisation represents a methodological breakthrough that can be deployed to a multitude of systems to navigate the intricate landscape of high-temperature superconductors and the broader realm of quantum materials in general.

Bulk measurements

Macroscopic properties of our $\text{Fe}(\text{Se}_{0.4\pm\alpha}, \text{Te}_{0.6\pm\beta})$ single crystal establish a baseline for its bulk behaviour. Figure 2a displays electrical resistivity against temperature, revealing the onset of a superconducting transition at 14.4 K. The temperature-dependent resistivity in the normal state serves as a means to distinguish between bulk and filamentary superconductivity in $\text{Fe}(\text{Se}, \text{Te})$.^{35,36} Our samples exhibit metallic temperature dependency above the superconducting, affirming bulk superconductivity devoid of excess Fe.³⁶ The low residual resistivity ($\sim 300 \mu\Omega\text{cm}$), which is among the lowest reported for $\text{Fe}(\text{Se}, \text{Te})$, combined with the sharpness of the transition and high transition temperature, underlines the high quality of our crystals.³⁶

Figure 2b illustrates magnetic field expulsion commencing at approximately 14.4 K, i.e. the manifestation of the shielding and Meissner effects. The zero-field-cooled (ZFC) susceptibility curve approaches a value of -1, indicative of nearly perfect diamagnetic shielding after accounting for geometrical factors.³⁷ In comparison the field-cooled (FC) susceptibility has a much smaller effect, and such low Meissner effects are generally attributed to strong pinning.

In addition, the superconducting volume fraction of crystals from the same process was found to be ca. 95-98%.³⁸

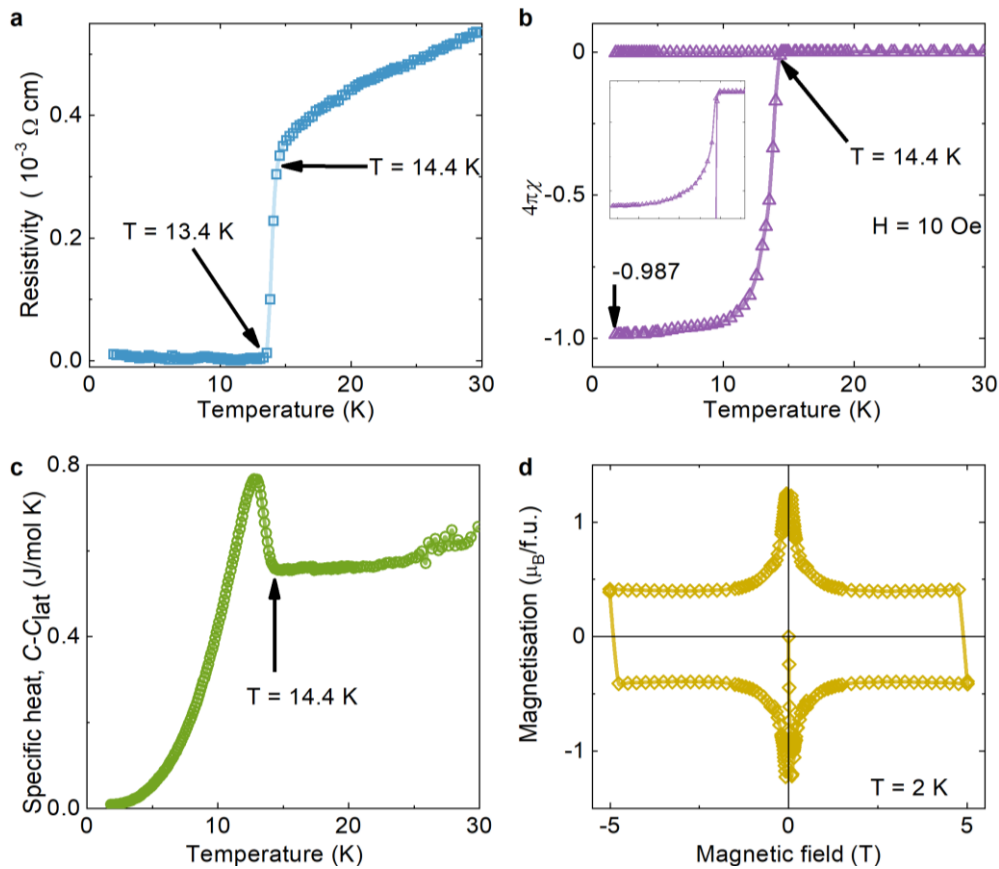


Figure 2 | Bulk superconductivity below ca. 14 K. **a**, Electrical resistivity plotted against temperature, featuring a sharp drop to zero starting at 14.4 K; data collected during heating in the absence of magnetic field. **b**, Temperature-dependent magnetic susceptibility measured using ZFC and FC methods, with a 10 Oe magnetic field. The data reveal a clear but small Meissner effect, with T_C onset of ~ 14.4 K, indicated by the arrow. At 2 K, the ZFC curve approaches -1, which is the expected value for 100% screening. **c**, Specific heat measurements after lattice background subtraction (see Methods section), displaying a distinct peak onset at around 14.4 K, indicative of a phase transition consistent with superconductivity. **d**, Field-dependent magnetization measured at 2 K, corroborating the attributes of a II-type superconductor.

Specific heat measurements, Figure 2c, further substantiate the bulk superconducting transition in our Fe(Se,Te) crystals. As elaborated in the supplementary material, Figure S1, applying a simple Debye approximation to our data in the 3-5 K range yields a residual Sommerfeld coefficient $\gamma_0 = 0.807$ mJ / mol K^2 . This low γ_0 , serves as additional evidence for the high quality of our crystals.³⁸ The $M(H)$ curve in Figure 2d provides yet more evidence for superconductivity, exhibiting the classic shape for type II superconductors. Utilizing the Bean model (Refs. ^{39,40}) and assuming our sample is a flat slab perpendicular to the magnetic field, we estimate critical currents on the order of 10^5 A/cm².

Spatially resolved measurements

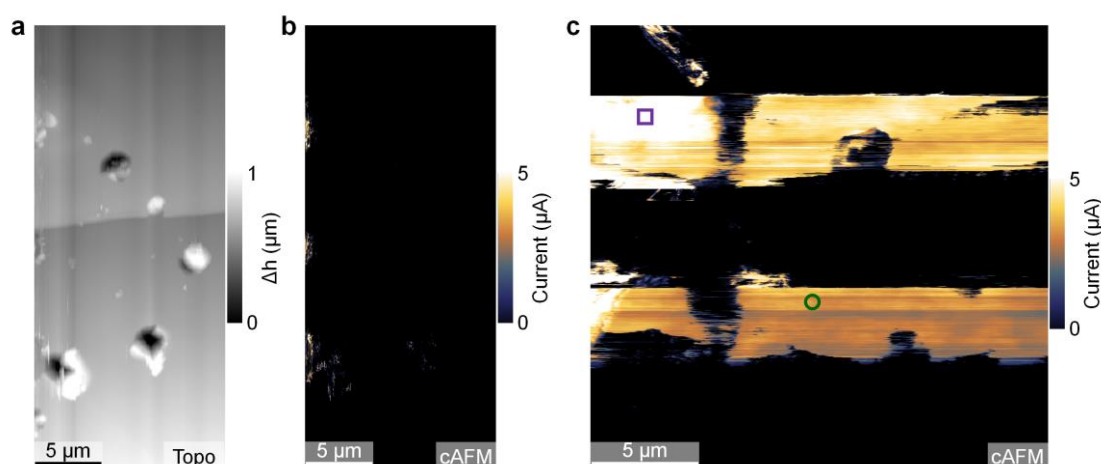


Figure 3 | Enhanced conductivity is spatially inhomogeneous at 1.5 K. **a**, Topographic image of the cleaved surface; height information is given by the false colours according to the scale bar. **b**, CAFM corresponding to **a**. For both **a** and **b**, the slow scan direction is horizontal and the pixel size is 15.5 nm. **c**, cAFM image of an adjacent area, showing areas of drastically enhanced conductivity and areas of no conductivity. The purple square indicates areas with a current of ca. 5.5 μA while the green circle shows areas of ca. 3.5 μA . The slow scan axis is vertical and the pixel size is 17 nm. Both **b** and **c** are collected with 100 mV applied between the sample and the back electrode, and the measured current is indicated by the false colours defined by the scale bars.

Taken together, the bulk data in Figure 2 suggest our sample is a high-quality homogeneous bulk superconductor. To directly measure the spatial distribution of these properties, we used cAFM. Figure 3a presents a topographical image of a freshly cleaved surface, captured at 1.5 K. Lighter shades correspond to elevated regions relative to the darker areas, confirming the sample's clean cleavage with only minor topographic variations. Figure 3b is the corresponding current measurements, obtained with an applied voltage of 100 mV between the tip and the back electrode. Lighter (yellow) regions indicate zones of heightened electrical current compared to the darker (black) areas. Contrary to expectations—based on the bulk data in Figure 2, it is immediately evident that majority of the sample surface does not conduct at these voltages. Importantly, this observation is not an isolated case but representative of multiple samples of $\text{Fe}(\text{Se}_{0.4\pm\alpha}, \text{Te}_{0.6\pm\beta})$ investigated with cAFM.

Some locations on the surface exhibit significantly enhanced conductivity, as in Figure 3c. Captured at 1.5 K with an applied voltage of 100 mV and a pixel size of 17 nm, this image reveals two parallel stripes of elevated conductivity. Intriguingly, areas with heightened conductivity can broadly be separated into two distinct current responses: for example, the region denoted by the purple square registers a current of approximately 5.5 μA , while the

green-circled area about $3.5 \mu\text{A}$. Similar ‘digitization’ of the current values has been observed across multiple samples and suggests that different spatial locations exhibit different superconducting properties, i.e. consistent with multiple gap states reported in other works focusing on macroscopic data collection.⁴¹ Critically, the cAFM data of Figure 3 unequivocally demonstrate that these apparently homogeneous bulk superconducting samples, at the micron scale, comprise multiple areas with distinct electrical properties.

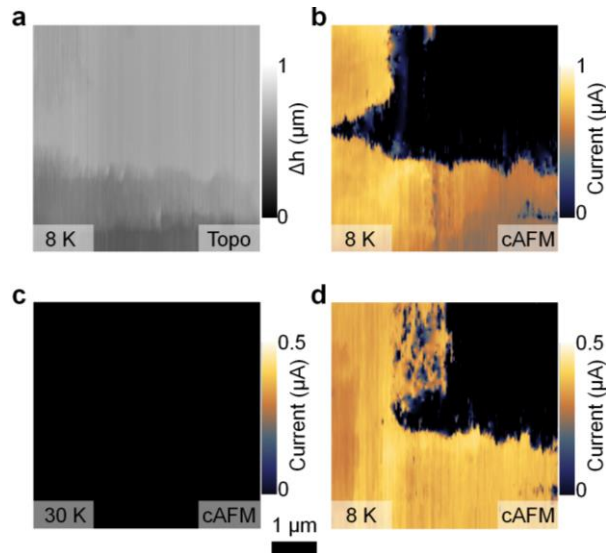


Figure 4 | Enhanced conductivity vanishes above T_c . **a**, Topographic image collected at 8 K; false colours indicate changes in height according to the scale on the right. **b**, Corresponding map of current variations; panels **a** and **b** are part of the same data set. **c**, Current variations in the same area, measured at 30 K: showing no measurable conductivity. **d**, Current recorded in the same region after subsequent cooling to 8 K. All scans have a pixel size of 15 nm, and their slow scan axis runs from left to right, and all images were aligned via their topography.

To elucidate the nature of the observed enhanced conductivity, we conducted cAFM measurements both above and below T_c . Figure 4a displays the topography of a selected region at 8 K, while Figure 4b presents the corresponding conductivity data, underscoring once again the sample's local inhomogeneity. When the same area is measured at 30 K, as illustrated in Figure 4c, the enhanced conductivity conspicuously vanishes, confirming its temperature-dependent nature. To validate the repeatability of these observations, we conducted a subsequent cAFM scan at 8 K using an applied voltage of 0.05 V (Figure 4d). The re-emergence of enhanced conductivity upon cooling below T_c corroborates that the observed enhanced currents are correlated with the superconducting state. Interestingly, a slight change in the extent of the superconducting regions was observed; we speculate this could be due to measurement induced changes to the local stoichiometry or structure of the sample.^{42,43} Note, all panels from Figure 4b-d are aligned based on their topographic images to ensure consistent

locations. In summary Figure 4 implies two significant points: first, that cAFM can measure superconductivity at the local level, and second, that Fe(Se,Te)-based systems possess a rich local microstructure even when their bulk properties appear homogeneous.

Atomic scale composition

Even when bulk properties appear homogeneous, cAFM reveals local variations in superconductivity suggesting that Fe(Se,Te)-based systems possess a rich microstructure, motivating the use of APT to test for difference in composition. We use a scanning electron microscope (SEM) to find the superconducting region identified in cAFM, and a superposition of these two images is given in Figure 5a. APT needles were prepared from the areas marked (1), (2) and (3) in Figure 5a, following the process detailed in the methods section. The 3D composition of the superconducting region (1) as measured by APT is presented in Figure 5b, and graphs of the compositions of the other two regions are in Figure 5c and d, respectively. The graphs in Figure 5c and d, resolve a relatively large difference in composition between the superconducting (3) and non-superconducting region (2), most notable is the change in iron to tellurium ratio. Interestingly excess iron has previously been reported to be detrimental to superconductivity in these systems on a bulk scale.³⁶

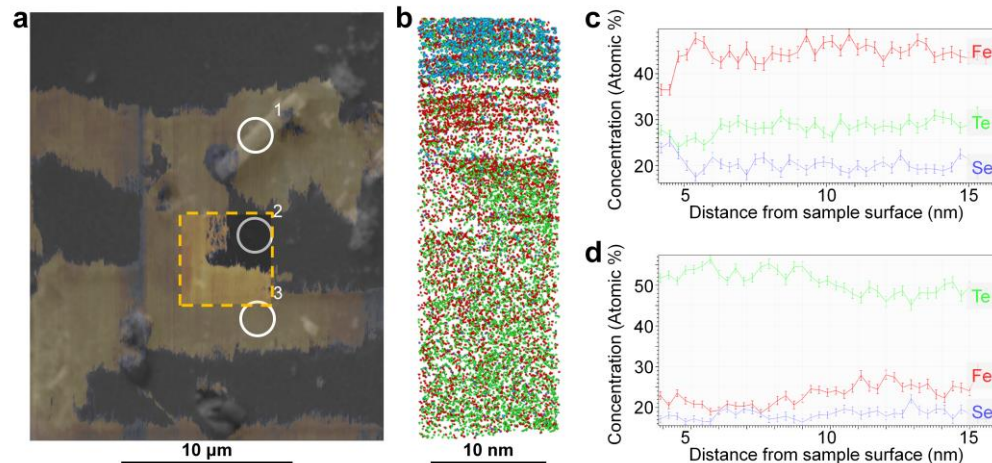


Figure 5 | Electron microscopy and atom probe microscopy. **a**, Is a superposition of an SEM and cAFM image, aligned via topography, showing the region of interest. The yellow box represents the area imaged in Figure 4, and the white circles indicate where APT needles were prepared. **b**, Atom map of composition from region 1: Fe (red), Te (green), Se (purple), O (blue). **c**, One-dimensional concentration profile of the non-superconducting region, created by integrating along an atomic map from region 2. **d**, One-dimensional concentration profile of the superconducting region, created by integrating along an atomic map from region 3.

To determine whether these compositional changes were associated with structural alterations, we employed scanning transmission electron microscopy (STEM), as shown in

Figure S2. Notably, we observed no differences between the superconducting and non-superconducting regions. In addition to emphasizing the value of cAFM in pinpointing these distinct areas, this highlights that the compositional nuances that driving superconductivity elude STEM, even when targeted across the phase interface. This might provide insight into why such heterogeneities have remained unreported to date.

Conclusions

Our study introduces a methodological innovation, bridging a critical gap in spatial resolution direct measurements of conduction in superconductors. Employing low temperature cAFM, we discovered that crystals, perceived as homogeneous through bulk techniques, can actually be dominated by distinct microstructural variations. By pinpointing areas of differing conduction, we strategically selected a superconducting region for atomic scale 3D compositional mapping, directly linking the electronic behaviour with specific atomic configurations. These insights emphasize the pivotal role microstructures can hold in type II superconductors. Beyond this specific realm, our research establishes cAFM as a crucial tool for direct multiscale characterization at low temperatures, setting the stage for richer understandings of complex quantum materials.

Experimental methods

Crystal growth

Single-phase crystals of $\text{FeSe}_x\text{Te}_{1-x}$ were synthesized via a self-flux method using the precursor elements— Fe (99.99% purity), Se (99.999%), and Te (99.999%)—both Se and Te were subjected to zone-refining to minimize oxide contaminants prior to the crystal growth. The synthesis and crystal growth was executed in hermetically-sealed double quartz ampoules. The preparation was done in two-steps. In the first step a mixture of the elements was slowly heated to 1100 °C, soaked for 72 h and then fast cooled to 410 °C and soaked again for 99 h. At the second step, material prepared at the first step was reground in an Ar glove box and filed in quartz ampoule, locked and transferred to pumping system. After pumping to 10^{-3} mbar the ampoule was sealed. At the second step, after a fast increase of temperature to 1100 °C, the ampoule was soaked for 72 h followed by slow cooling (6 °C/h) to 410 °C, where final soak for an extended 100-hour period was done. The process was culminating in quenching in a water-ice bath. Elemental stoichiometry was confirmed through EDX, while phase purity was checked on crushed samples via X-ray powder diffraction, employing a STADI-P diffractometer (STOE & CIE) with a position-sensitive detector and CuK_α radiation ($\lambda = 1.540560 \text{ \AA}$). For

comprehensive analytical details, we refer the reader to previous work by Tsurkan et al. Ref ³⁸ and other characterisations of crystals from the same batch are given by Refs. ^{11,44,45}.

Scanning probe microscopy

The low-temperature scanning probe microscopy (SPM) measurements were conducted with an attoAFM I atomic force microscope (attocube systems AG, Haar, Germany). Boron-doped single-crystal diamond tips (AD-2.8-AS, radius: 10 nm; Bruker France, Wissembourg, France) were employed for these experiments. Prior to measurements, the vacuum chamber was evacuated to pressures below 10^{-5} mbar and subsequently purged with helium; this evacuation-purge cycle was executed thrice at ambient conditions. A controlled atmosphere was maintained by introducing helium at a few millibars as an exchange gas. The sample underwent cooling to liquid helium temperatures over a multi-hour period, following our normal protocols.

Sample preparation involved retrieval a virgin crystal from a sealed quartz tube, followed by the fresh cleavage of both crystal facets using a razor blade. One facet was subsequently anchored to an attocube sample holder using a silver conductive paste. The entire preparation procedure—comprising quartz tube breach, crystal cleavage, sample mounting, and chamber evacuation—was expediently completed within an eight-minute timeframe to preclude atmospheric contamination. Several different samples, from the same batch used for bulk measurements, were investigated with the cAFM: all showed a predominantly insulating surface with only local islands of enhanced conductivity.

All the SPM images were analysed and processed using the open source software “Gwyddion”.⁴⁶ The only processing of the data was changing the colour, setting the scale, and correcting horizontal scars; the latter being routine for the fast scan direction of an SPM image. All images in Figures 3 and 4 have been cropped, so they fit as display items. None of these made any quantifiable change to raw data and all original (.bcrf) files are available upon reasonable request to the corresponding author.

Bulk data collection

Temperature dependent resistivity was measured on a freshly cleaved sample using the resistivity option of Physical Property Measurements System (PPMS, Quantum Design) with four electrical contacts made using conducting silver paint. The specific heat was measured on the same equipment. The magnetic susceptibility and magnetisation data was measured using a superconducting quantum interface devices (SQUID, MPMS-5, Quantum Design) with a field cooled and zero field cooled protocol. The SQUID measurements were repeated for several different crystals from this batch and no variation in magnetic properties was observed.

Atom probe tomography

Samples were opened in a N₂ environment glove-box, mounted onto a copper stub and placed in an atom probe puck (Cameca) for transfer purposes. This was transferred under UHV to Side 1 of a dual puck stage plate (Oxford Atomic) inside a Thermo-Fisher Scientific Helios Hydra 5 CX PFIB using a Ferrovac Vacuum Cryo Vacuum Module for site specific APT sample preparation. A commercially available highly Sb-doped single-crystal silicon micro post array (CAMECA Instruments Inc., Madison, WI, USA) was mounted on a Cu clip, placed into an atom probe puck and loaded in ambient conditions into Side 2 of the dual puck stage plate. This dual puck approach allows the easy transfer of air sensitive substrates into the PFIB and the removal of sharpened APT samples with minimal transfer stages. The sites of interest were removed from the bulk material using Xe⁺ plasma of the Helios 5 CX Hydra and similar PFIB conditions as in reference ⁴⁷. Once the milled-out region was mounted and welded to the top of the post, the sample was sharpened to an apex diameter < 100 nm using 30 kV Xe⁺ from 1 to 30 pA, and polishing using 5 kV Xe⁺ ions at 30 pA to remove regions severely damaged by the higher energy ions as in ref. ⁴⁸. The samples were then transferred in UHV to the LEAP via the Ferrovac suitcase and analysed in a Cameca LEAP 5000 XR (Local Electrode Atom Probe equipped with reflection) using laser pulsing conditions of 30 pJ, 140-200 kHz and 50 K base temperature. APT data reconstruction and analysis were performed using CAMECA Integrated Visualization and Analysis Software (IVAS) as part of AP Suite 6.

Scanning tunnelling electron microscopy imaging

Omniprobe copper-based lift-out TEM grid was mounted in a clamp holder and placed in an atom probe puck. This was then transferred to the PFIB via the Ferrovac suitcase. An electron transparent cross-section was prepared using Xe⁺ plasma based on the recipe in ref. ⁴⁹ and with a final polish using Ar 2kV. The puck with TEM lamella was then transferred back to the N₂ glovebox and then transferred to a Melbuild double tilt liquid nitrogen vacuum transfer TEM holder.

STEM imaging was performed using a Thermo-Fisher Scientific probe corrected mono X-FEG Spectra operated at 300 kV accelerating voltage. The convergence angle for ADF STEM imaging was 31 mrad with a measured fluorescent screen current was ~ 30 pA.

Manuscript

A large language model, ChatGPT, was used for proof reading of the manuscript text.

Acknowledgements

D.M.E. acknowledges and thanks funding from the Deutsche Forschungsgemeinschaft (grant No. EV 305/1-1). M.C. acknowledges funding from the Royal Society Tata University Research Fellowship (URF\R1\201318) and the EPSRC NAME Programme Grant

EP/V001914/1. M.C., J.O.D, B.G., are grateful for funding from the EPSRC under the grant EP/V007661/1. D.C., L.Pr. and V.T. acknowledge the support by the Deutsche Forschungsgemeinschaft (DFG, German Research Foundation) TRR 360-492547816 and via Project No. ANCD 20.80009.5007.19 (Moldova).

References

1. Fernandes, R. M. *et al.* Iron pnictides and chalcogenides: a new paradigm for superconductivity. *Nature* **601**, 35–44 (2022).
2. Böhmer, A. E. & Kreisel, A. Nematicity, magnetism and superconductivity in FeSe. *J. Phys. Condens. Matter* **30**, 23001 (2018).
3. Zhou, X. *et al.* High-temperature superconductivity. *Nat. Rev. Phys.* **3**, 462–465 (2021).
4. Party like it's LK-99. *Nat. Phys.* **19**, 1222 (2023).
5. Garisto, D. Claimed superconductor LK-99 is an online sensation — but replication efforts fall short. *Nature* **620**, 253 (2023).
6. Lee, S. *et al.* Superconductor $\text{Pb}_{10-x}\text{Cu}_x(\text{PO}_4)_6\text{O}$ showing levitation at room temperature and atmospheric pressure and mechanism. (2023).
7. Lee, S., Kim, J.-H. & Kwon, Y.-W. The First Room-Temperature Ambient-Pressure Superconductor. (2023).
8. Garisto, D. LK-99 isn't a superconductor — how science sleuths solved the mystery. *Nature* **620**, 705–706 (2023).
9. Kohsaka, Y. *et al.* How Cooper pairs vanish approaching the Mott insulator in $\text{Bi}_2\text{Sr}_2\text{CaCu}_2\text{O}_{8+\delta}$. *Nature* **454**, 1072–1078 (2008).
10. Lang, K. M. *et al.* Imaging the granular structure of high- T_c superconductivity in underdoped $\text{Bi}_2\text{Sr}_2\text{CaCu}_2\text{O}_{8+\delta}$. *Nature* **415**, 412–416 (2002).
11. Singh, U. R. *et al.* Spatial inhomogeneity of the superconducting gap and order parameter in $\text{FeSe}_{0.4}\text{Te}_{0.6}$. *Phys. Rev. B* **88**, 155124 (2013).
12. Cho, D., Bastiaans, K. M., Chatzopoulos, D., Gu, G. D. & Allan, M. P. A strongly inhomogeneous superfluid in an iron-based superconductor. *Nature* **571**, 541–545 (2019).
13. Sprau, P. O. *et al.* Discovery of orbital-selective Cooper pairing in FeSe. *Science* (80-

-). **357**, 75–80 (2017).
14. Singer, A. *et al.* Nucleation of dislocations and their dynamics in layered oxide cathode materials during battery charging. *Nat. Energy* **3**, 641–647 (2018).
 15. Jäck, B., Xie, Y. & Yazdani, A. Detecting and distinguishing Majorana zero modes with the scanning tunnelling microscope. *Nat. Rev. Phys.* **3**, 541–554 (2021).
 16. Herrera, E. *et al.* Quantum-well states at the surface of a heavy-fermion superconductor. *Nature* **616**, 465–469 (2023).
 17. Evans, D. M. *et al.* Strain relaxation behaviour of vortices in a multiferroic superconductor. *J. Phys. Condens. Matter* **31**, 135403 (2019).
 18. Puntigam, L. *et al.* Strain Driven Conducting Domain Walls in a Mott Insulator. *Adv. Electron. Mater.* **8**, (2022).
 19. Gault, B. *et al.* Atom probe tomography. *Nat. Rev. Methods Prim.* **1**, 51 (2021).
 20. Evans, D. M., Garcia, V., Meier, D. & Bibes, M. Domains and domain walls in multiferroics. *Phys. Sci. Rev.* **5**, 335–369 (2021).
 21. Mizuguchi, Y., Tomioka, F., Tsuda, S., Yamaguchi, T. & Takano, Y. Substitution effects on FeSe superconductor. *J. Phys. Soc. Japan* **78**, 74712 (2009).
 22. Kreisel, A., Hirschfeld, P. J. & Andersen, B. M. On the remarkable superconductivity of fese and its close cousins. *Symmetry (Basel)*. **12**, (2020).
 23. Tegel, M., Löhnert, C. & Johrendt, D. The crystal structure of $\text{FeSe}_{0.44}\text{Te}_{0.56}$. *Solid State Commun.* **150**, 383–385 (2010).
 24. Dioguardi, A. P. *et al.* NMR evidence for inhomogeneous glassy behavior driven by nematic fluctuations in iron arsenide superconductors. *Phys. Rev. B* **92**, 165116 (2015).
 25. Rinott, S. *et al.* Tuning across the BCS-BEC crossover in the multiband superconductor $\text{Fe}_{1+y}\text{Se}_x\text{Te}_{1-x}$: An angle-resolved photoemission study. *Sci. Adv.* **3**, e1602372 (2017).
 26. Homes, C. C., Dai, Y. M., Wen, J. S., Xu, Z. J. & Gu, G. D. $\text{FeTe}_{0.55}\text{Se}_{0.45}$: A multiband superconductor in the clean and dirty limit. *Phys. Rev. B* **91**, 144503 (2015).
 27. Chatzopoulos, D. *et al.* Spatially dispersing Yu-Shiba-Rusinov states in the unconventional superconductor $\text{FeTe}_{0.55}\text{Se}_{0.45}$. *Nat. Commun.* **12**, 298 (2021).
 28. Liu, C. *et al.* Zero-energy bound states in the high-temperature superconductors at the

- two-dimensional limit. *Sci. Adv.* **6**, eaax7547 (2020).
29. Machida, T. *et al.* Zero-energy vortex bound state in the superconducting topological surface state of Fe(Se,Te). *Nat. Mater.* **18**, 811–815 (2019).
 30. Yin, J. X. *et al.* Observation of a robust zero-energy bound state in iron-based superconductor Fe(Te,Se). *Nat. Phys.* **11**, 543–546 (2015).
 31. Wang, Z. *et al.* Topological nature of the FeSe_{0.5}Te_{0.5} superconductor. *Phys. Rev. B* **92**, 115119 (2015).
 32. Wang, Z. *et al.* Evidence for dispersing 1D Majorana channels in an iron-based superconductor. *Science (80-.)*. **367**, 104–108 (2020).
 33. Lubashevsky, Y., Lahoud, E., Chashka, K., Podolsky, D. & Kanigel, A. Shallow pockets and very strong coupling superconductivity in FeSe_xTe_{1-x}. *Nat. Phys.* **8**, 309–312 (2012).
 34. Shibauchi, T., Hanaguri, T. & Matsuda, Y. Exotic superconducting states in FeSe-based materials. *J. Phys. Soc. Japan* **89**, 102002 (2020).
 35. Liu, T. J. *et al.* From ($\pi,0$) magnetic order to superconductivity with (π,π) magnetic resonance in Fe_{1.02}Te_{1-x}Se_x. *Nat. Mater.* **9**, 716–720 (2010).
 36. Sun, Y., Shi, Z. & Tamegai, T. Review of annealing effects and superconductivity in Fe_{1+y}Te_{1-x}Se_x superconductors. *Supercond. Sci. Technol.* **32**, 103001 (2019).
 37. Campbell, A. M., Blunt, F. J., Johnson, J. D. & Freeman, P. A. Quantitative determination of percentage superconductor in a new compound. *Cryogenics (Guildf)*. **31**, 732–737 (1991).
 38. Tsurkan, V. *et al.* Physical properties of FeSe_{0.5}Te_{0.5} single crystals grown under different conditions. *Eur. Phys. J. B* **79**, 289–299 (2011).
 39. Bean, C. P. Magnetization of hard superconductors. *Phys. Rev. Lett.* **8**, 250–253 (1962).
 40. Bean, C. P. Magnetization of high-field superconductors. *Rev. Mod. Phys.* **36**, 31–39 (1964).
 41. Cho, K. *et al.* Precision global measurements of London penetration depth in FeTe_{0.58}Se_{0.42}. *Phys. Rev. B* **84**, 174502 (2011).
 42. Evans, D. M. *et al.* Observation of Electric-Field-Induced Structural Dislocations in a Ferroelectric Oxide. *Nano Lett.* **21**, 3386–3392 (2021).

43. Evans, D. M. *et al.* Conductivity control via minimally invasive anti-Frenkel defects in a functional oxide. *Nat. Mater.* (2020) doi:10.1038/s41563-020-0765-x.
44. Singh, U. R. *et al.* Evidence for orbital order and its relation to superconductivity in $\text{FeSe}_{0.4}\text{Te}_{0.6}$. *Sci. Adv.* **1**, e1500206 (2015).
45. Wahl, P., Singh, U. R., Tsurkan, V. & Loidl, A. Nanoscale electronic inhomogeneity in $\text{FeSe}_{0.4}\text{Te}_{0.6}$ revealed through unsupervised machine learning. *Phys. Rev. B* **101**, 115112 (2020).
46. Nečas, D. & Klapetek, P. Gwyddion: An open-source software for SPM data analysis. *Cent. Eur. J. Phys.* **10**, 181–188 (2012).
47. Thompson, K. *et al.* In situ site-specific specimen preparation for atom probe tomography. *Ultramicroscopy* **107**, 131–139 (2007).
48. Douglas, J. O., Conroy, M., Giuliani, F. & Gault, B. In Situ Sputtering From the Micromanipulator to Enable Cryogenic Preparation of Specimens for Atom Probe Tomography by Focused-Ion Beam. *Microsc. Microanal.* **29**, 1009–1017 (2023).
49. Vitale, S. M. & Sugar, J. D. Using Xe Plasma FIB for High-Quality TEM Sample Preparation. *Microsc. Microanal.* **28**, 646–658 (2022).

Supplementary Information

Considering the simple Debye approximation for specific heat, $C = \gamma T + \beta T^3$, where γ is the Sommerfeld coefficient, related to the electronic contributions, and β represents the contribution from the lattice we can replot our specific heat data in the form C / T vs T^2 . Below 5 K where the simple Debye plot is considered reasonable, a linear fit gives values of $\gamma_0 = 0.807$ mJ / mol K^2 and $\beta = 0.393$. Note that in this data there appears to be an additional contribution appears below 3 K, which may originate from a measurement artifact.

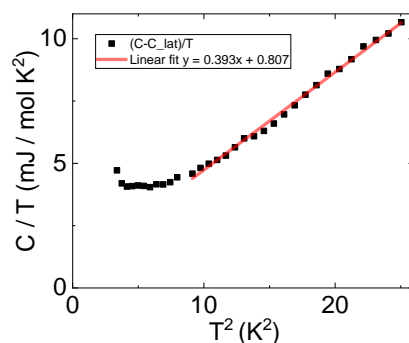


Figure S1 | Temperature dependence of specific heat. The y-axis intercept, 0.807 mJ/mol K^2 , gives the value of γ_0 in a simplistic Debye situation.

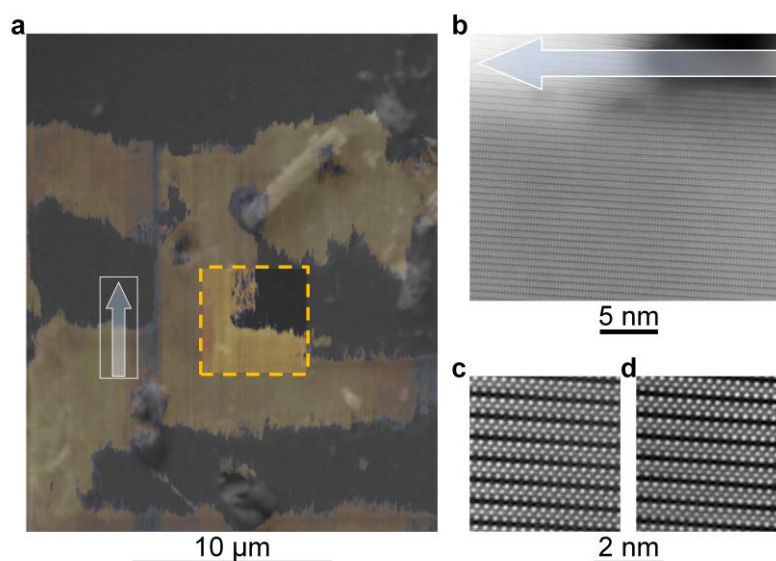


Figure S2 | Scanning transmission electron microscopy. **a**, The same SEM and cAFM data from Figure 5a. The black box, with transparent arrow, indicates where the electron transparent lamella was prepared from. **b**, STEM across the lamella, with the non-conducting area at the head of the arrow and the highly conducting area at the tail of the arrow. **c**, is a higher magnification STEM image from the non-superconducting region, marked by the arrowhead in **a**. **d**, is a higher magnification from the superconducting, below the tail of the arrow. This data shows no clear change in atomic structure between the two regions.